PCCP

Substituted SrFeO3 as Robust Oxygen Sorbents for Thermochemical Air Separation: Correlating Redox Performance with Compositional and Structural Properties

Journal:	*Physical Chemistry Chemical Physics*
Manuscript ID	CP-ART-01-2020-000275.R2
Article Type:	Paper
Date Submitted by the Author:	25-Mar-2020
Complete List of Authors:	Krzystowczyk, Emily; North Carolina State University, Chemical Engineering Wang, Xijun; North Carolina State University Dou, Jian; North Carolina State University, Chemical Engineering Haribal, Vasudev; North Carolina State University, Chemical and Biomolecular Engineering Li, Fanxing; North Carolina State University, Chemical Engineering

ARTICLE

Substituted $SrFeO_3$ as Robust Oxygen Sorbents for Thermochemical Air Separation: Correlating Redox Performance with Compositional and Structural Properties

Emily Krzystowczyk,[a*] Xijun Wang, [a*] Jian Dou, [a] Vasudev Haribal, [a] Fanxing Li [a]

Received 00th January 20xx,
Accepted 00th January 20xx

DOI: 10.1039/x0xx00000x

Thermochemical air separation via cyclic redox reactions of oxide-based oxygen sorbents has the potential to achieve high energy efficiency. Although a number of promising sorbents have been investigated, further im-provements in sorbent performance through fundamental understanding of the structure-performance rela-tionships are highly desirable. In this study, we systematically investigated the effects of A and B site dopants on the oxygen uptake/release properties (i.e., vacancy formation energy, reduction enthalpy, oxygen release temperature, and oxygen capacity) of SrFeO3 family of perovskites as oxygen sorbents. A monotonic correlation between DFT calculated oxygen vacancy formation energy and oxygen release temperature demonstrates the effectiveness of DFT for guiding sorbents selection. Combining vacancy formation energy with stability analy-sis, dopants such as Ba and Mn have been identified for tuning redox property of $SrFeO_3$ sorbent, and increas-ing the oxygen capacity for temperature and pressure swings when compared to undoped $SrFeO_3$. The Mn doped sample was proved to be highly stable, with less than a 3% decrease in capacity over 1000 cycles. Alt-hough the dynamic nature of the redox process makes it difficult to use a single vacancy formation energy as the descriptor, a systematic approach was developed to correlate the oxygen storage capacities with the sorbents' compositional properties and vacancy formation energies. The combination of DFT calculations with experimental studies from this study provides a potentially effective strategy for developing improved sorbents for thermochemical air separation.

Introduction

Market revenue of oxygen and nitrogen from air separation currently exceeds $38.8 billion and is expected to reach $48.8 billion by 2023[1,2]. Besides the increasing O_2 demand in the conventional manufacturing sector, emerging technologies such as oxyfuel combustion for CO_2 capture are likely to further spur industrial O_2 consumption within the near future. According to the Carbon Dioxide Information Analysis Center, from 2000 to 2013, fossil fuel combustion consumed 30.55 Gt of O_2 with the market continuing to grow[1,3–6]. Among the various approaches for oxygen production, cryogenic air separation is the most prevalent, with commercial plants producing more than 5,000 tonnes per day[7]. Although the technology is well-demonstrated and extensively optimized, its thermodynamic second law efficiency is still limited to ~25% due to the intrinsic limitations for cryogenic distillation[8]. As such, the high cost and energy intensity for O_2 production from conventional, cryogenic ASU can make the cost for CO_2 capture via oxyfuel combustion prohibitive. Because of the desire to reduce emissions, there is an increasing need improve energy efficiency for air separation. Chemical looping air separation (CLAS), which separates oxygen from the air via cyclic redox reactions of an oxide based oxygen sorbent, represents a promising method for oxygen production[9–13]. A recent simulation study estimated that the CLAS system consumes 0.05 and 0.07 kWh/ton O2 in electricity[14–16]. In comparison, state-of-the-art cryogenic ASU requires 0.21 kWh/ ton O_2. This corresponds to a 71.4% increase in efficiency[17]. The CLAS system can be operated in a variety of ways, with the two most common being (i) multiple series of packed bed reactors with varying partial pressures to separate the oxygen from air (Figure 1), or (ii) two reactors, one for oxidation in air and one for oxygen release (reduction) using steam or CO_2 as the fluidizing medium, with an oxygen carrier moving between the two reactors[18–21]. The key to further improve the efficiency and economic attractiveness of CLAS resides in the performance of oxygen sorbents and hence the need to rationally tune a sorbent to increase stability and oxygen carrying capacity, adjust to a more desirable operating pressure range, and decrease operating temperatures is paramount.

[a] Department of Chemical and Biomolecular Engineering
North Carolina State University
NC 27606 (USA)

† Footnotes relating to the title and/or authors should appear here.
Electronic Supplementary Information (ESI) available: [details of any supplementary information available should be included here]. See DOI: 10.1039/x0xx00000x

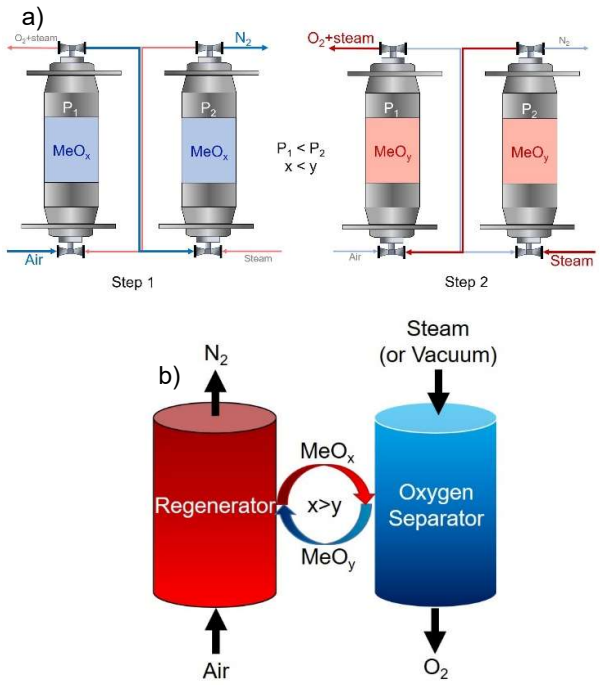

Figure 1. (a) Packed bed configuration of the chemical looping air separation (CLAS) system. Each reactor is filled with oxygen sorbent and oxygen is separated via pressure swing. (b) Two bed reactor configuration for CLAS. The reactors are held at different pressures and/or temperatures with oxygen sorbent circulating between the reactor beds.

Oxygen sorbents investigated to date include mono or bimetallic oxides containing Cu-, Co-Fe-, Mn-, as well as perovskite-structured mixed oxides[22–24]. Studies have shown that Cu containing oxides require high operating temperatures (> 800 °C), leading to a high energy penalty and reactor cost [25–29]. Mn oxides, on the other hand, could operate at lower temperatures (< 650 °C) from a thermodynamic standpoint, however, the reaction rates are very slow under such conditions [6,26,26,27]. The need to balance the redox thermodynamics and kinetics at lower operating temperatures has led to studies of perovskites for CLAS[14,30,31].

Perovskites can be tailored to exhibit excellent flexibility in reversibly creating oxygen vacancies under P_{O2} and temperature swings, at relatively low temperatures[5]. The ability of perovskite oxides to conduct and donate lattice oxygen (O^{2-}) at relatively low temperatures (e.g. <650 °C) and their flexibility/tunability to accommodate various dopants are central to CLAS[32–35]. Although a number of recent studies have provided very useful insights on the effect of dopants[5,25–27,32–36], further understanding of rationally and quantitatively tuning perovskites' properties are highly desirable. While iron oxides themselves are not suitable for CLAS, recent studies indicated that Fe containing perovskites, especially those with a $SrFeO_3$ parent structure, possess attractive redox properties for CLAS. [36–38] It is noted that $SrFeO_3$ materials still face challenges such as limited oxygen carrying capacity. Moreover, the oxygen partial pressures required for oxygen generation are relatively low. As such, significant steam purge or vacuum are needed for O_2 generation. For instance, undoped $SrFeO_3$ showed 0.2 w.t.% oxygen capacity under an oxygen partial pressure swing of 0.05 to 0.2 atm at 700 °C. Partial substitution of Sr with Ca can improve redox properties of the $SrFeO_3$ based oxygen sorbent by improving oxygen capacity up to 1.1 w.t.% at the same conditions above, although the long term stability and steam resistance of the sorbent were not established[5,39]. Moreover, most previous studies used extremely low PO_2 (<0.001%) to enhance O_2 release. Such an oxygen partial pressure is not practical from an application standpoint due to the needs for significant purge steam. Though many studies have been reported on doped $SrFeO_3$ materials[25,36,39], there is still a lack of systematic study on the effects of A site and B site dopants on the oxygen vacancy formation, oxygen transport kinetics, and long-term stability for air separation applications.

In this study, several promising A and B site dopants were selected based on thermodynamic and empirical criteria such as reduction temperature and structure tolerance factor. Specifically, Ba, Y, La, and K were selected as A-site dopants whereas Mn, Co, Cu, and Ni were selected as B site dopant. In general, adding dopants increased the oxygen donation properties at all temperatures and partial pressures, and long-term studies were conducted on the best performing samples. From results determined by DFT and in conjunction with experiments, a correlation between oxygen vacancy formation energies and initial oxygen release temperatures were obtained. Furthermore, DFT calculated oxygen vacancy dependent formation energy was successfully used to predict and compare oxygen capacity of sorbents under a pressure swing air separation mode. The long term stability of doped $SrFeO_3$ sorbent was also established over 1000 redox cycles.

Experimental Section

Synthesis Method A or B site doped perovskites (i.e., $Sr_{1-x}A_xFe_{1-y}B_yO_3$, A = K, Y, Ca, and Ba, B = Mn, Co, Ni, Cu) were synthesized using a sol-gel method. In a typical synthesis of $Sr_{0.9}K_{0.1}FeO_3$, 9 mmol of $Sr(NO_3)_2$ was dissolved in 15 ml of deionized water, followed by adding 1 mmol of KNO_3 and 10 mmol of $Fe(NO_3)_3.9H_2O$. After that, 50 mmol (2.5:1 citric acid to total mol of cations) of citric acid was added to the solution and stirred at room temperature for 30 min. Then, 4.2 ml of ethylene glycol was added, and the solution was heated at 80 °C for 3 h under well stirring. After that, the formed gel was heated in oven at 120 °C for 16 h. The dried sample was further heated in air at 1000 °C for 8 h to remove the organic template and form the perovskite phase. Finally, the remaining sample was sieved to a desired particle size range, between 150 μm and 250 μm.

TGA Experiments Program was devised to ramp the temperature to 700 °C at 20 °C /min and hold the temperature for 5 minutes at a constant oxygen partial pressure on a TA SDT Q650 and Q550. The temperature is then decreased in a step like manner by 450 °C in 50 °C increments. Then, the oxygen partial pressure is changed, and the temperature is ramped back to 700 °C (Figure S1). The initial start temperature was chosen to be high in order to increase the kinetics at each temperature. Oxygen partial pressures were chosen to be 20%, 5%, and 1% balance argon as chemical potential is proportional to the log of the partial pressure. These pressures were recorded on a Setnag oxygen analyzer and controlled using MFCs.

Temperature programed desorption (TPD) was done by heating the sample to 1000 ºC at a rate of 5 ºC / min in Ar in the TA SDT Q650 and Q550. Initial temperature of reduction was determined by finding the first peak in the temperature vs derivative weight loss curve. The results for each dopant is presented in Figure S2.

Optimal sample was chosen to be heated to 600 ºC and programed to undergo 1000 redox cycles in the presence of steam. This was done on the same TGA as mentioned above with the addition of approximately 2% steam. During the oxidation step, 20% O_2 balance Ar was flown to the sample for a period of 3 minutes, as oxidation is commonly being known to be the faster of the two steps. During the reduction step, 100% argon is flown for 7 minutes.

δ values for the perovskites were determined based on $\delta = \frac{\Delta m M_w}{m M_O} + \delta(0)$ where Δm is the change in mass during the redox reaction, M_w is the molar mass of the sample at the initial redox state, m is the initial mass, and M_o is the molecular weight of oxygen. δ(0) is the initial non-stoichiometry at ambient temperatures and oxygen partial pressures. It was determined by heating the sample to 1000 ºC under a high PO_2. The gas was then switched to 20% H_2 balance Ar to fully reduce the sample and kept at 1000 C until weight stabilized. δ(0)was then determined based on the decomposition reactions. For example, $SrFeO_{3-\delta}$ was determined using the equation $\delta(0) = \frac{2M_O - 3xM_O - x(M_{Sr}+M_{Fe})}{(1-x)M_O}$.

Characterization Crystal structures of the samples were determined using a Rigaku SmartLab X-ray diffractometer with Cu Kα (k = 0.1542 nm) radiation operating at 40 kV and 44 mA. A scanning range of 20–80° (2h) with a step size of 0.05 holding for 3 s at each step was used. XRD patterns were identified using HighScore Plus.

Density Functional Theory First-principles simulations were performed at the DFT level implemented by the Vienna ab initio simulation package (VASP)[40] with the all-electron projector augmented wave (PAW) model[41] and Perdew-Burke-Ernzerhof (PBE) functions[42]. A kinetic energy cutoff of 450 eV was used for the plane-wave expansion of the electronic wave function. The convergence criterions of force and energy were set as 0.01 $eVÅ^{-1}$ and 10^{-5} eV, respectively. A Gaussian smearing of 0.1 eV was applied for optimization. A 2 × 1 × 2 Gamma-centered k-point grid was chosen for the Brownmillerite ($Sr_8Fe_8O_{20}$) and the lattice-redefined Perovskite ($Sr_8Fe_8O_{24}$) unit cell which contains 36 atoms. In our simulations the 2 × 1 × 1 Brownmillerite ($Sr_{16}Fe_{16}O_{40}$) and Perovskite ($Sr_{16}Fe_{16}O_{48}$) supercell were used with two out of 16 Sr or Fe atoms replaced by A or B site dopant to mimic the doped materials, where A represents Ba or Y and B represents Cu or Mn. The strong on-site coulomb interaction on the d-orbital electrons of the transition metals were treated with the GGA+U approach[43]. The U_{eff} of Fe, Mn and Cu were set as 4, 3.9 and 4 eV, which were shown to give reasonable predictions of both geometric and electronic structures in previous studies[44]. To make the calculations directly comparable, we assumed a ferromagnetic (FM) state for all the cases. Previous studies indicated that magnetic ordering had relatively small effect on the oxygen vacancy formation and migration[45]. The Gibbs free energy was calculated as:$G = H - TS = E_{DFT} + E_{ZPE} - T(S_{vib} + S_{conf})$. Here E_{DFT}, E_{ZPE}, S_{vib} and S_{conf} represent the DFT total energy, zero-point energy, vibrational and configurational entropy respectively. The vibrational and configurational entropy were calculated based on[33]:

$$S_{vib} = R\sum_i \left(\frac{h\nu_i/kT}{\exp(h\nu_i/kT) - 1} - \ln[1 - \exp(-h\nu_i/kT)]\right)$$

$$S_{conf} = aR \cdot [\ln(0.5 - \delta) - \ln\delta]$$

where R is the ideal gas constant, h is the Plank constant, ν_i is the frequency of the i^{th} vibrational mode, a is a factor referring to the interaction of oxygen vacancies with a=2 describing an ideal solid solution with no defect interaction. We also considered the cases when a=1 and 3, which corresponds to different extent of vacancy-vacancy interactions, but found that their impacts on the Gibbs free energies are too small (< 0.05 eV) to affect our conclusions. Therefore a=2 was chosen in this study.

Results and Discussion

Dopant Selection To perform a systematic study on dopant effect, we used the thermodynamic data from the Materials Project as a tool, in conjunction with the tolerance number, to guide the initial dopant selection[46]. Figure 2 maps oxygen sorbents based on reduction enthalpy and tolerance factor. B site elements are comprised of transition metals (i.e., Mn, Co, Ni, Cu), which tailor the reduction potentials. For example, with Sr as A site element, the oxidation enthalpy of perovskites with different B site element has the following trend of $SrCuO_3 \approx SrCoO_3 < SrFeO_3 < SrMnO_3$, consistent with the oxygen affinity of respective transition metals. A site dopants (i.e., Ba, La, Y, K) are selected based on desired charge and ionic radius, which, when combined with the transition metal, empirically determine the stability of the compound based on the Goldschmidt Tolerance Factor. For air separation application, the oxygen bonding with perovskite has to be low enough to be released at relatively low temperature (i.e., at < 700 ºC), while high enough for the oxide to be reoxidized in air.

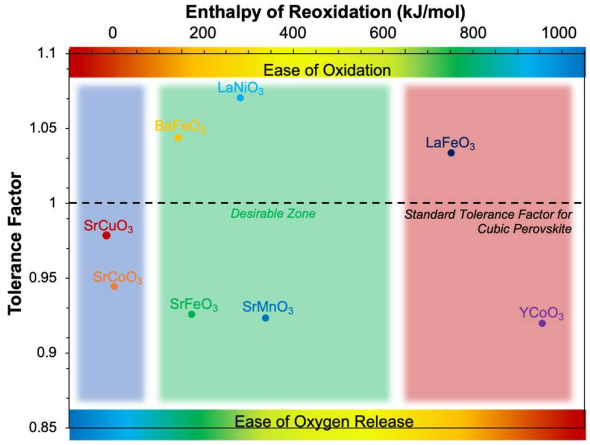

Figure 2. Selection of dopants based on reduction temperature and tolerance factor. Enthalpy calculated using the Materials Project and the reduction from the perovskite phase (ABO_3) to the brownmillerite phase ($ABO_{2.5}$)

Experimental Screening Based on Figure 2, Ni and La were chosen due to their potential to increase the oxidation enthalpy (which has a negative correlation to reduction enthalpy) while increasing the tolerance factor when compared to $LaFeO_3$ and $SrFeO_3$. As pure $SrCuO_3$ and $SrCoO_3$ are extremely unstable and will reduce to alternative phases and lose the ability for oxygen uptake into the lattice (i.e., reduction temperature < 0 ºC), Co, and Cu were added to decrease the oxidation enthalpy of doped $SrFeO_3$ sorbents. Ba, Mn and Y were chosen to either increase or decrease

tolerance factor of the doped perovskite oxygen sorbents. Summary of anticipated dopant effects on enthalpy and tolerance factor are found in Table 1. Each sample was characterized using XRD to confirm the primary phase being consistent with the SrFeO3 parent structure (Figure S3-S6). Although small amount of phase impurities (<3%) were observed in a few doped samples, these phase impurities are not anticipated to contribute to the CLAS reactions (see Figure S3-S6 and discussions). Dopant incorporation into the unit cell was verified by XRD. Slightly smaller 2θ angles for the primary perovskite phase after Ba, La, and Mn addition indicate an increase in unit cell size, while slightly higher 2θ angles after Co, Cu, K, Ni, and Y indicate cell contraction (Table S1).

Table 1. Net anticipated effect of dopant species on $SrFeO_3$.

Cation Species	Anticipated Effect on Ease of Oxygen Release	Anticipated Effect on Tolerance Factor
Ba	Neutral	+
La	+	+
Y	+	-
K	Unknown	+
Mn	+	-
Ni	+	+
Co	-	+
Cu	-	+

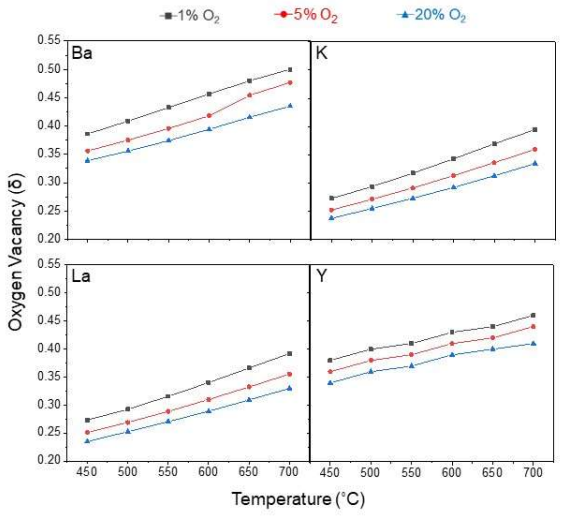

Figure 3. Effect of A site dopant on oxygen vacancy (δ) of $Sr_{0.9}A_{0.1}FeO_{3-\delta}$ in 1-20% O_2 and at 450-700 ºC. See $SrFeO_3$ screening in Figure S7.

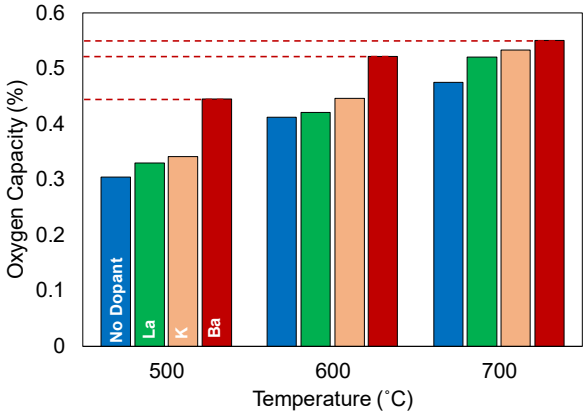

Figure 4. Isothermal oxygen capacity for $Sr_{0.9}K_{0.1}FeO_3$, $Sr_{0.9}Ba_{0.1}FeO_3$, $Sr_{0.9}La_{0.1}FeO_3$, and $SrFeO_3$ for oxygen partial pressures between 20% and 1% O_2 balance Ar.

The effect of A site dopants on oxygen vacancy of doped $SrFeO_{3-\delta}$ oxygen sorbents are summarized in Figure 3, showing how δ changes with respect to temperature and pressure for $SrFeO_3$ doped with Y, K, Ba, and La. The Ba doped sample showed the highest oxygen capacity, with a δ change of 0.17 between 20% O2 at 450 ˚C and 1% O_2 at 700 ˚C. Isothermal weight loss was 0.54 w.t.% at 700 ˚C, isobaric weight loss was 0.96 w.t.% from 450 to 700 ˚C in 1% O_2. As a comparison, the $SrFeO_3$ sample showed a change in δ of 0.138 and an isobaric weight loss of 0.8% for the same conditions, which is notably lower than the Ba doped sample. Figure 4 also supports this trend, as at each temperature (i.e., 500, 600, and 700 ˚C), the Ba doped sample showed the highest isothermal oxygen capacity from a pressure swing.

However, a trend noticed in the two figures above indicates that the incremental oxygen capacity for the Ba-doped sample decreases as temperature increases, which is evident in the distance between dashed lines on Figure 4, correlating to an increase in oxygen capacity of 11.06% from 450-500 ˚C and of 0.92% from 650-700 ˚C. Meanwhile, the La and K samples consistently gain capacity at higher temperatures, correlating to an increase in δ relative to the Ba- doped sample. This indicates that Ba doping would be more beneficial to increase capacity for lower temperature applications, and La and K doping would be more suitable for applications at or above 700 ºC. $BaFeO_3$ has the desired reduction enthalpy and temperature based on calculations using The Materials Project, indicating that doping Ba at the A site enables similar properties to their respective pure metal perovskites. This demonstrates the importance of selection a proper A site dopant to fine tune the redox behavior of $SrFeO_3$ sorbent, which can be tailored for air separation applications under different temperature ranges.

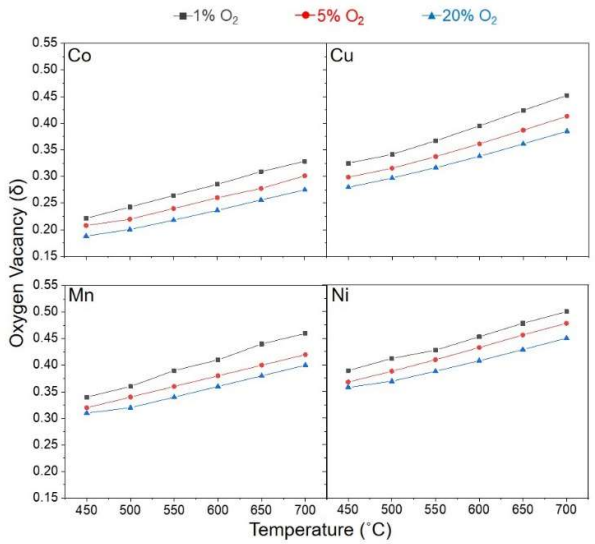

Figure 5. Effect of B site dopant on oxygen vacancy (δ) of $SrFeO_3$ in 1, 5%, and 20% O_2 at temperatures between 450-700 ºC. See $SrFeO_3$ screening in Figure S2.

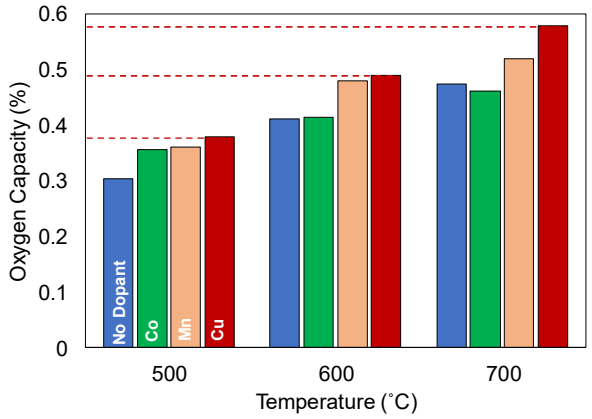

Figure 6. Temperature vs oxygen capacity for $SrFe_{0.9}Mn_{0.1}O_3$, , $SrFe_{0.9}Co_{0.1}O_3$, $SrFe_{0.9}Cu_{0.1}O_3$and $SrFeO_3$ when oxygen partial pressure is varied between 20% and 1%.

Figure 6 shows B site dopants of Mn, Co, Ni, and Cu on SrFeO3 tested to determine how δ changes with respect to temperature and pressure. Based on the oxygen vacancy study, it is evident that $SrFe_{0.9}Mn_{0.1}O_3$ and $SrFe_{0.9}Cu_{0.1}O_3$ have the highest oxygen capacity across the temperature ranges (i.e., 450-700 ºC) tested. For example, the maximum δ change of 0.17 for Cu doped samples was measured from 1% O_2 at 700 ºC to 20% O_2 at 450 ºC, corresponding to an oxygen storage capacity of 1.47 w.t.%. The Cu sample showed an isothermal weight loss of 0.58 w.t.% at 700 ºC and an isobaric weight loss (at 1% O2 between 450-700 ºC) to be 1.09 w.t.%. Comparatively, the Mn sample showed a maximum δ shift of 0.16 and an isothermal weight loss of 0.5 w.t.% and isobaric weight loss of 1% at the same conditions listed above. Cu, though unlike the Ba sample, consistently increases its capacity as the temperature increases, and has higher capacity than Ba at 700 ºC. However, at all other temperatures investigated, the Ba sample has the highest capacity at all temperature and pressure swings.

Table 2. Maximum δ changes from temperature (450 ºC - 700 ˚C) and pressure swing (20%-1%) for each dopant

Dopant	Maximum Δδ	Capacity (w.t.%)
none	0.14	1.03
Ba	0.17	1.35
K	0.16	1.37
La	0.16	1.30
Y	0.12	0.99
Co	0.14	1.19
Cu	0.17	1.47
Mn	0.15	1.33
Ni	0.14	1.22

Dopants of Ba, Cu, and Mn have shown to significantly increase oxygen capacity when compared to $SrFeO_3$. This result is further evaluated using DFT calculations, as discussed below.

DFT Analysis of the Dopant Effect DFT calculations were performed to obtain the relationships between the oxides' compositional and structural properties with redox performance. From a thermodynamic standpoint, there are two aspects closely related to oxygen sorbent performance (i) the ease of initial oxygen release; (ii) oxygen capacity under a certain oxygen partial pressure and/or temperature swing. The ease of initial oxygen release is related to the energy for oxygen vacancy creation at low vacancy concentrations, whereas we anticipate the oxygen capacity to be determined by the dynamic relationships between vacancy concentration and vacancy formation energy. Although many recent publications have correlated the vacancy formation energy from a perfect supercell with its oxygen capacity, more accurate estimation of an oxide's oxygen capacity requires systematic investigation of vacancy formation energy as a function of the vacancy concentration. Our study indicates that ease of initial oxygen release correlates well to initial oxygen release temperature, as indicated by TPR (Figure 7). However, it has poor correlation with the working oxygen capacity. Generally, reduction temperature decreases with lowering initial vacancy formation energy. For example, La doped $SrFeO_3$ has a vacancy formation energy of 0.43 eV, corresponding to a first reduction peak at a temperature of 856 ºC. By changing the dopant to Mn or Ba, the vacancy formation energy decreases to 0.22 and 0.11 eV, respectively. As a result, the reduction temperature shifts to 387 ºC and 295 ºC, suggesting easier oxygen release at low temperatures. The negative vacancy formation energy of K, Co, and Cu doped $SrFeO_3$ suggests that these sorbents are prone to release oxygen at even lower temperatures.

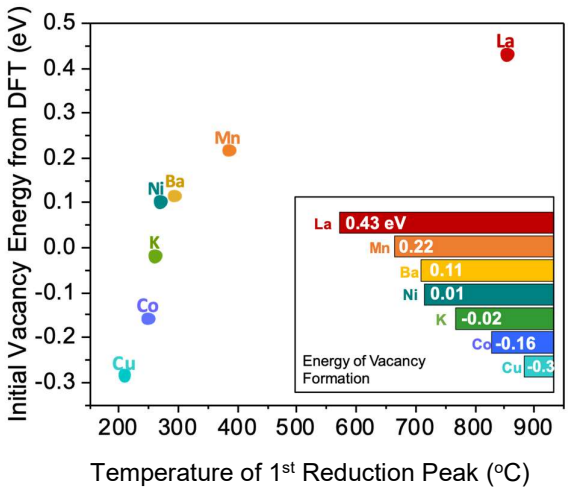

Figure 7. Correlation between DFT calculated initial vacancy formation energy (ΔE_V) and reduction temperature obtained from first reduction peak in a temperature programmed reduction (TPR) study for doped $SrFeO_3$ sorbents (see Figure S3 for TPR data).

We note that the initial vacancy formation energy, while being an excellent predictor for the onset of oxygen release, does not directly link with the experimentally obtained oxygen capacity. This is understandable since the measurement of oxygen capacity of the experimental samples do not start from defect-free status, and both vacancy concentration and vacancy formation energy would change under oxygen partial pressure swings in CLAS. As such, an optimal oxygen carrier should demonstrate a suitable level of vacancy formation energy (corresponding to P_{O2} swing) within a reasonably large span of vacancy concentration (corresponding to oxygen capacity). To further understand this, phase transitions of $SrFeO_3$ from perovskites (cubic) to Brownmillerite (orthorhombic) were investigated first, in order to ensure an accurate base structure is used for the calculation of the oxides' thermodynamic parameters. To determine the relative phase stability at different oxygen vacancy concentration levels (δ), we calculated the Gibbs free energies of the oxides using DFT by both (i) removing oxygen from the perovskite structure; and (ii) adding oxygen to the Brownmillerite structure (Figure S8-S11, Table S2). The relative energy of the two cases at an identical oxygen vacancy concentration level would then determine the more stable form of the structure. As seen in Figure 8, the energy associated with these two phases intersected at $\delta \approx 0.26$, indicating the phase transition of the perovskite to Brownmillerite structure would occur at $\delta > 0.26$, this is in general agreement with a previous literature report[47]. We note that the δ values for all the perovskites we investigated were larger than 0.3 under working conditions at 700 °C. Therefore, to more accurately reproduce the experimental observed δ changes for all the A- and B-doped species, we used Brownmillerite instead of perovskite as our starting point.

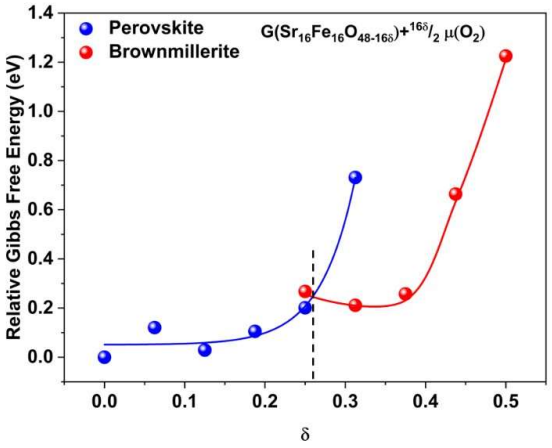

Figure 8: Computed relative Gibbs free energies of $SrFeO_3$ perovskite (blue) and brownmillerite (red) at different δs under 700 °C. The intersection indicates a possible critical point of phase transition.

For the reaction $ABO_{3-\delta_1} \rightarrow ABO_{3-\delta_2} + \frac{\delta_2-\delta_1}{2}O_2$, the thermodynamic favorability can be described by Gibbs free energy change $\Delta G_{\delta 1 \rightarrow \delta 2}$. The ΔG for the δ change in 0.25~0.3125, 0.3125~0.375, 0.375~0.4375 and 0.4375~0.5 were computed at 700 °C (Figure S12 and S13). However, since the experimentally observed δ values for each species are between 0.32 and 0.49 at all temperatures tested, we pick $\Delta G_{0.375 \rightarrow 0.4375}$ as an indicator for the experimental oxygen capacity as shown in Figure 9. A higher ΔG indicates less favourable oxygen release within this δ range. Therefore, the trend of predicted oxygen capacity should follow the trend of Y < SF < Ba < Mn < Cu, which agrees well with the experimental findings (Y < SF < *Mn*< *Ba* < Cu) except for the relative values of Ba and Mn, which are likely to be within the computational errors. Compared to computing vacancy formation energy at a fixed δ (e.g. perfect supercell), the DFT analysis above provides a potentially more accurate approach to computationally predict working oxygen capacity for perovskite-structured sorbents.

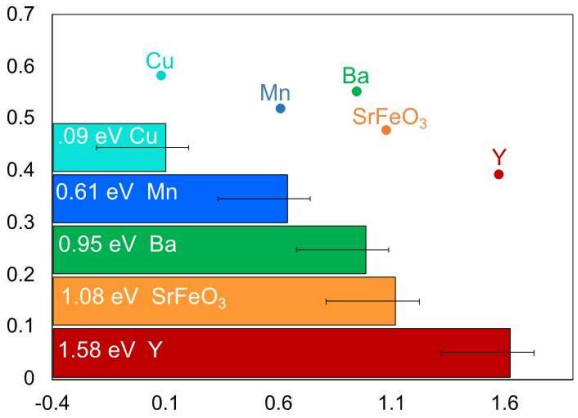

Figure 9. DFT calculated ΔG at δ changes from 0.375 to 0.4375 for Cu, Mn, Ba, $SrFeO_3$ and Y doped materials at 700 °C; Oxygen capacity as a function of temperature for $Sr_{0.9}Y_{0.1}FeO_3$, $SrFeO_3$, $SrFe_{0.9}Mn_{0.1}O_3$, and $Sr_{0.9}Fe_{0.1}FeO_3$ from pressure swing between 20 and 1% O_2.

Long Term Studies While Cu doped materials had higher capacities based on experimental results, concerns associated with agglomeration and need for higher temperatures led us to not consider this sample for long term studies[27,48]. As the Ba-doped sample showed high capacity and proved to be the more thermodynamically viable material, it was further investigated. The sample underwent 1000 redox cycles, with each cycle comprised of a 2-minute oxidation in simulated air and a 4-minute reduction in Ar. The gas delivery was sent through a bubbler at room temperature to deliver approximately 2% steam to determine stability over many cycles for practical applications. The sample capacity decreased 10.4% between the first cycle and the last cycle. As this indicates that the sample is not robust enough to be practically applicable, another sample was chosen to undergo long term testing.

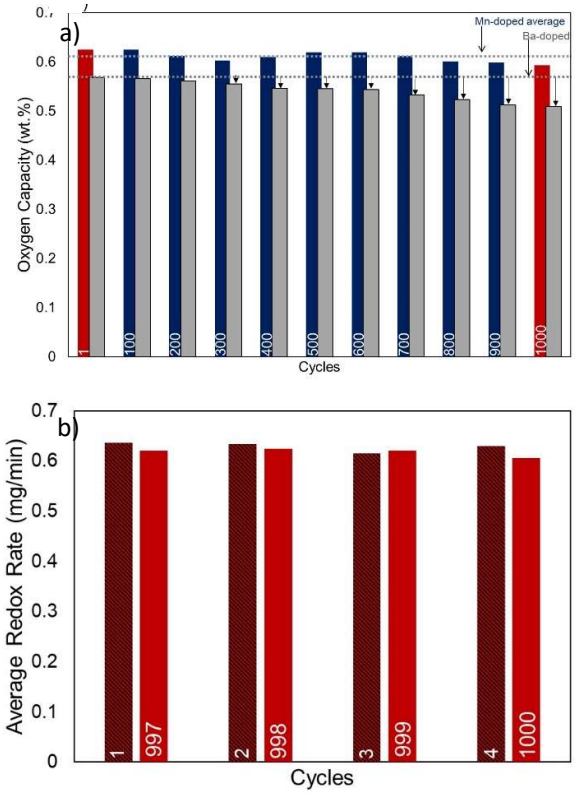

Figure 10. A. Oxygen capacity during the 1000 cycle run for $SrFe_{0.9}Mn_{0.1}O_3$ compared to oxygen capacity every 100 cycles of $Sr_{0.9}Ba_{0.1}FeO_3$. Blue line indicates average capacity across 1000 cycles for Mn-doped sample. Grey line initial oxygen capacity for Ba-doped sample. Oxygen capacity was tested every 100 cycles during the run and calculated based on an average of 3 runs (see Figure S14, S15 and S16). B. Average redox rate of first four cycles vs last four cycles of the Mn-doped sample.

The Mn doped sample was chosen due to its high oxygen capacity and for environmental, agglomeration, and expense concerns of using Cu as dopant. In this experiment, the Mn-doped sample underwent 1000 redox cycles, with each cycle comprised of a 4-minute oxidation in simulated air and a 6-minute reduction in Ar based on preliminary TA results (Figure S11). Reduction and oxidation rates were studied based on time to reach 0.5% weight change for the sample. When comparing the rates and capacity for the Mn- doped sample between the first four cycles (cycle 1,2,3, and 4) with the last four cycles (cycle 997, 998, 999, 1000), the rates are similar (i.e., 0.061%/min vs 0.06%/min), showing little signs of deactivation. This indicates that the sample is incredibly robust, as it is able to withstand 1000 cycles with only a 2.5% capacity loss and little loss in redox reaction rates. Additionally, with the introduction of steam, little to no deactivation was noticed and no side phases were formed as noticed in the XRD characterization comparing the fresh and cycled samples (Figure S17). SEM imaging of the pre and post cycled material showed no agglomeration of elements (Figure S18 and S19) and decreases in particle size (Figure S20), though as indicated above led to no change in capacity or kinetics (Figure 16). This robustness, even when subjected to steam over multiple cycles, proves that $SrFe_{0.9}Mn_{0.1}O_3$ would be a suitable oxygen carrier for CLAS.

Conclusions

In this work, A site dopants including Ba, K, Y and La and B site dopants of Mn, Co, Cu, and Ni were investigated to determine if the dopants were able to contribute qualities of the pure metal oxides to tailor $SrFeO_3$ to be more suited for chemical looping air separation. Dopants of Ba on the A site increased capacity by 0.16% in a redox scheme and Cu on the B site increased capacity by 0.29% when compared to the base material- $SrFeO_3$. This increase in capacity was understood through thermodynamic evaluation in conjunction with DFT calculations on the energy required to remove oxygen at varying oxygen vacancies, indicating that in the desired ΔH, only the Ba sample was able to release oxygen. The Mn sample, another high-performance dopant, underwent 1000 redox cycles between 20% O2 and Ar, and showed 2% degradation in capacity and little change in kinetics, proving that the material is robust.

Conflicts of interest

There are no conflicts to declare

Acknowledgements

This work was supported by the U.S. Department of Energy (Award No. FE0031521), the National Science Foundation (Grant No. CBET-1510900), the Nagoya University – NC State Research Collaboration Seed Grants, and the North Carolina State University Kenan Institute for Engineering, Technology, and Science. We acknowledge the use of the Analytical Instrumentation Facility (AIF) at North Carolina State University, which is supported by the State of North Carolina and the National Science Foundation.

Reference

1 R. and M. ltd, Air Separation Plant Market by Process (Cryogenic, Non-Cryogenic), Gas (Nitrogen, Oxygen, Argon), End User (Iron & Steel, Oil & Gas, Chemical, Healthcare), Region - Global Forecast to 2026, https://www.researchandmarkets.com/reports/4047220/air-separation-plant-market-by-process, (accessed 18 July 2019).

2 Oxygen Market 2019 Industry Growth, Size, Share, Global Forecasts Analysis, Company Profiles, Competitive Landscape and Key Regions Analysis Research Report, https://www.nbc29.com/story/40740560/oxygen-market-2019-industry-growth-size-share-global-forecasts-analysis-company-profiles-competitive-landscape-and-key-regions-analysis-research, (accessed 9 September 2019).
3 B. Moghtaderi, *Energy Fuels*, 2010, **24**, 190–198.
4 J. Dou, E. Krzystowczyk, A. Mishra, X. Liu and F. Li, *ACS Sustainable Chem. Eng.*, 2018, **6**, 15528–15540.
5 J. Vieten, B. Bulfin, F. Call, M. Lange, M. Schmücker, A. Francke, M. Roeb and C. Sattler, *Journal of Materials Chemistry A*, 2016, **4**, 13652–13659.
6 J. Vieten, B. Bulfin, M. Senholdt, M. Roeb, C. Sattler and M. Schmücker, *Solid State Ionics*, 2017, **308**, 149–155.
7 C. Windmeier, M. J. Kirschner, A. Alekseev, S. Dowy, M. Grahl, L. Jansson, P. Keil, G. Lauermann, M. Meilinger, W. Schmehl and H. Weckler, 2017, pp. 1–32.
8 G. Rochelle, E. Chen, S. Freeman, D. Van Wagener, Q. Xu and A. Voice, *Chemical Engineering Journal*, 2011, **171**, 725–733.
9 Q. Imtiaz, D. Hosseini and C. R. Müller, *Energy Technology*, 2013, **1**, 633–647.
10 S. Remsen and B. Dabrowski, *Chem. Mater.*, 2011, **23**, 3818–3827.
11 Y. Aoki, K. Kuroda, S. Hinokuma, C. Kura, C. Zhu, E. Tsuji, A. Nakao, M. Wakeshima, Y. Hinatsu and H. Habazaki, *J. Am. Chem. Soc.*, 2017, **139**, 11197–11206.
12 T. Motohashi, Y. Hirano, Y. Masubuchi, K. Oshima, T. Setoyama and S. Kikkawa, *Chem. Mater.*, 2013, **25**, 372–377.
13 B. Bulfin, J. Lapp, S. Richter, D. Gubàn, J. Vieten, S. Brendelberger, M. Roeb and C. Sattler, *Chemical Engineering Science*, 2019, **203**, 68–75.
14 H. Song, K. Shah, E. Doroodchi, T. Wall and B. Moghtaderi, *Energy & Fuels*, 2014, **28**, 1284–1294.
15 K. Shah, B. Moghtaderi, J. Zanganeh and T. Wall, *Fuel*, 2013, **107**, 356–370.
16 Y. Chen, N. Galinsky, Z. Wang and F. Li, *Fuel*, 2014, **134**, 521–530.
17 M. Sorgenfrei and G. Tsatsaronis, *Applied Energy*, 2014, **113**, 1958–1964.
18 X. P. Dai, J. Li, J. T. Fan, W. S. Wei and J. Xu, *Industrial & Engineering Chemistry Research*, 2012, **51**, 11072–11082.
19 P. Hallberg, D. Jing, M. Rydén, T. Mattisson and A. Lyngfelt, *Energy & Fuels*, 2013, **27**, 1473–1481.
20 M. Rydén, A. Lyngfelt and T. Mattisson, *International Journal of Greenhouse Gas Control*, 2011, **5**, 356–366.
21 T. Zhang, Z. Li and N. Cai, *Korean Journal of Chemical Engineering*, 2009, **26**, 845–849.
22 A. Lyngfelt, *Applied Energy*, 2014, **113**, 1869–1873.
23 A. Lyngfelt, B. Leckner and T. Mattisson, *Chemical Engineering Science*, 2001, **56**, 3101–3113.
24 A. Fossdal, E. Bakken, B. A. Øye, C. Schøning, I. Kaus, T. Mokkelbost and Y. Larring, *International Journal of Greenhouse Gas Control*, 2011, **5**, 483–488.
25 J. Vieten, B. Bulfin, D. E. Starr, A. Hariki, F. M. F. de Groot, A. Azarpira, C. Zachäus, M. Hävecker, K. Skorupska, N. Knoblauch, M. Schmücker, M. Roeb and C. Sattler, *Energy Technology*, , DOI:10.1002/ente.201800554.
26 N. Galinsky, A. Mishra, J. Zhang and F. Li, *Applied Energy*, 2015, **157**, 358–367.
27 N. Galinsky, M. Sendi, L. Bowers and F. Li, *Applied Energy*, 2016, **174**, 80–87.
28 N. L. Galinsky, Y. Huang, A. Shafiefarhood and F. Li, *ACS Sustainable Chem. Eng.*, 2013, **1**, 364–373.
29 J. E. Readman, A. Olafsen, Y. Larring and R. Blom, *Journal of Materials Chemistry*, 2005, **15**, 1931.
30 I. Adánez-Rubio, P. Gayán, A. Abad, L. F. de Diego, F. García-Labiano and J. Adánez, *Energy Fuels*, 2012, **26**, 3069–3081.
31 T. Mattisson, E. Jerndal, C. Linderholm and A. Lyngfelt, *Chemical Engineering Science*, 2011, **66**, 4636–4644.
32 K. Wang, Q. Yu and Q. Qin, *J Therm Anal Calorim*, 2013, **112**, 747–753.
33 J. Vieten, B. Bulfin, P. Huck, M. Horton, D. Guban, L. Zhu, Y. Lu, K. A. Persson, M. Roeb and C. Sattler, *Energy & Environmental Science*, 2019, **12**, 1369–1384.
34 C. Y. Lau, M. T. Dunstan, W. Hu, C. P. Grey and S. A. Scott, *Energy Environ. Sci.*, 2017, **10**, 818–831.
35 M. T. Dunstan, A. Jain, W. Liu, S. Ping Ong, T. Liu, J. Lee, K. A. Persson, S. A. Scott, J. S. Dennis and C. P. Grey, *Energy & Environmental Science*, 2016, **9**, 1346–1360.
36 B. Bulfin, J. Vieten, D. E. Starr, A. Azarpira, C. Zachäus, M. Hävecker, K. Skorupska, M. Schmücker, M. Roeb and C. Sattler, *Journal of Materials Chemistry A*, 2017, **5**, 7912–7919.
37 A. Khare, D. Shin, T. S. Yoo, M. Kim, T. D. Kang, J. Lee, S. Roh, I.-H. Jung, J. Hwang, S. W. Kim, T. W. Noh, H. Ohta and W. S. Choi, *Advanced Materials*, 2017, **29**, 1606566.
38 Y. Mao and S. S. Wong, *Advanced Materials*, 2005, **17**, 2194–2199.
39 N. Miura, H. Ikeda and A. Tsuchida, *Ind. Eng. Chem. Res.*, 2016, **55**, 3091–3096.
40 P. E. Blöchl, *Phys. Rev. B*, 1994, **50**, 17953–17979.
41 J. P. Perdew, K. Burke and M. Ernzerhof, *Phys. Rev. Lett.*, 1996, **77**, 3865–3868.
42 G. Kresse and J. Furthmüller, *Phys. Rev. B*, 1996, **54**, 11169–11186.
43 V. I. Anisimov, J. Zaanen and O. K. Andersen, *Phys. Rev. B*, 1991, **44**, 943–954.
44 G. Hautier, S. P. Ong, A. Jain, C. J. Moore and G. Ceder, *Phys. Rev. B*, 2012, **85**, 155208.
45 Y.-L. Lee, J. Kleis, J. Rossmeisl and D. Morgan, *Phys. Rev. B*, 2009, **80**, 224101.
46 A. Jain, G. Hautier, S. P. Ong, C. J. Moore, C. C. Fischer, K. A. Persson and G. Ceder, *Phys. Rev. B*, 2011, **84**, 045115.
47 J. Mizusaki, *Journal of Solid State Chemistry*, 1992, **99**, 162–172.

48 L. F. de Diego, F. García-Labiano, J. Adánez, P. Gayán, A. Abad, B. M. Corbella and J. María Palacios, *Fuel*, 2004, **83**, 1749–1757.

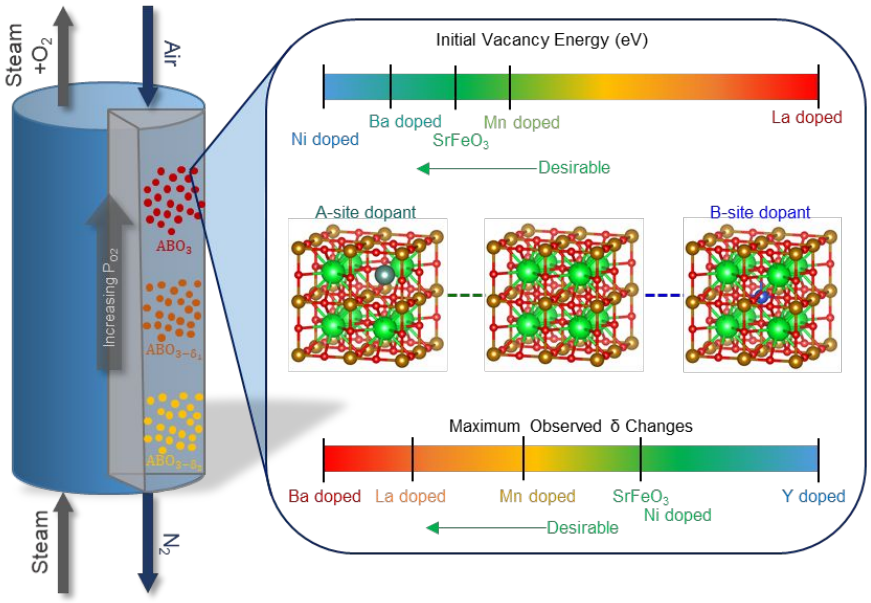

Quantification of the dopant effect on $SrFeO_3$ provides a potentially effective strategy for developing improved sorbents for thermochemical air separation.